Tailoring broadband acoustic energy suppression characteristics of double porosity metamaterials with compression constraints and mass inclusions

Shichao Cui and Ryan L. Harne[a)]

Department of Mechanical and Aerospace Engineering, The Ohio State University, Columbus, Ohio 43210, USA

A metamaterial that capitalizes on a double porosity architecture is introduced for controlling broadband acoustic energy suppression properties. When the metamaterial is subjected to static compressive stress, a global rotation of the internal metamaterial architecture is induced that softens the effective stiffness and results in a considerable means to tailor wave transmission and absorption properties. The influences of mass inclusions and compression constraints are examined by computational and experimental efforts. The results indicate that the mass inclusions and applied constraints can significantly impact the absorption and transmission properties of double porosity metamaterials, while the appropriate utilization of the underlying poroelastic media can further magnify these parametric influences. Based on the widespread implementation of compressed poroelastic media in applications, the results of this research uncover how internal metamaterial architecture and constraints may be exploited to enhance engineering noise control properties while using less poroelastic material mass. © 2017 Acoustical Society of America.
[http://dx.doi.org/10.1121/1.4986745]

[MRH]

I. INTRODUCTION

Suppressing structure- and fluid-borne acoustic waves has been a recurring motivation for numerous researchers in recent decades.[1] Because noise is often a pollutant to human health,[2] the desire to be isolated from unwanted acoustic energy has stimulated efforts to develop structures and materials with ever greater capabilities to suppress acoustic wave travel over a wide frequency range and without strict reliance upon the mass law.[3] The variety of systems devised to achieve these challenging goals is diverse. Considering several examples, mass-spring vibration neutralizers are shown to be effective for wave control in narrow frequency ranges near resonances,[4] metallic periodic structures may be designed for wide and deep bandgaps in elastic wave transmission,[5] while internal resonating lattice structures provide vibration absorption phenomena at targeted frequencies.[6] Because a minimum penalty of added mass is desirable to enhance wave attenuation for many engineering contexts, the more notable added mass incurred through the concepts surveyed above poses potential concern.

Motivated by such lightweighting demands, researchers have intently studied the acoustic absorption and transmission properties of porous media such as poroelastic foams.[1] Efforts have revealed increased wave absorption by rigid mass inclusions in foam layers,[7] and have found that arrangements of periodic resonant inclusion arrays may further enhance acoustic wave attenuation.[8,9] In addition, the mass inclusion shapes tailor the natural frequency,[10] which correspondingly tune the absorption properties.[7] These studies reveal a large influence of the solid mass inclusions on the ability of the material system to attenuate acoustic waves, albeit at the cost of heavier noise control solutions.

Interestingly, introducing a second manifestation of porosity into a porous material may improve absorption coefficient under certain circumstances by the *removal* of mass, particularly when the pores are parallel to the wave propagation direction.[11–14] Detailed studies of double porosity poroelastic layers have revealed the roles of multi-layering and variation of the porosity in order to modify sound attenuation properties, such as by leveraging periodic void patterns.[15] Indeed, similar periodic void patterns are shown to be critical toward the collapse of elastic metamaterials under compressive loads or constraints,[16–18] even potentially yielding large elastic[19] and vibroacoustic[20] energy dissipation characteristics. Geometric constraints and compression are regularly applied to poroelastic materials in practice,[11] which suggests that double porosity-based metamaterials may exhibit compression-dependent acoustic properties, possibly resulting in a means to tailor the significance of acoustic energy dissipation. Moreover, the numerous observations that mass inclusions in bulk poroelastic materials can manipulate the acoustic wave attenuation characteristics indicate that the incorporation of mass inclusions in double porosity materials may be another avenue for controlling wave energy transfer.

Considering the aforementioned works, there is a clear opportunity to advance fundamental understanding of double porosity metamaterials by exploring the roles of constraints and mass inclusions on governing the acoustic wave attenuation properties. Therefore, in this research we study a model metamaterial that integrates principles of double porosity,

---

a)Electronic mail: harne.3@osu.edu

constraint and collapse, and internally resonant mass inclusions to establish a deep knowledge on the opportunities realized at the intersection. Because each feature has individually been shown to be influential toward tailoring the absorption and transmission characteristics of metamaterials, the hypothesis of this research is that the integration of mass in and constraint on double porosity metamaterials may introduce new potential for the manipulation of acoustic characteristics such as absorption coefficient, transmission loss (TL), and force transmissibility (FT). Moreover, due to the advantages of reduced mass for material systems intended to suppress wave propagation, this research provides an assessment of how significantly additional mass inclusions contribute to the wave attenuation properties.

This report is organized in the following parts. Section II describes the design and fabrication steps undertaken to realize the double porosity metamaterial architecture and inclusions. After a mechanical properties characterization in Sec. II A, the results of experimental FT evaluations are presented in Sec. III A to exemplify significant means to control the passage of broadband elastic wave energy via the new double porosity metamaterials. Computational and experimental results of absorption coefficient and TL characteristics of the metamaterials are then presented in Secs. III B, III C, and III D in order to assess the roles of constraint and mass inclusion on such properties. Next, a finite element (FE) study is presented in Sec. III E to examine the intricate influences of added mass and applying constraint within different poroelastic materials that compose the metamaterial architecture. Finally, discussions and conclusions are provided in Sec. IV to summarize the findings.

II. DESIGN AND FABRICATION OF METAMATERIAL SPECIMENS

For a two-dimensional (2D) porous structure with periodic circular voids and constant cross section through a thickness dimension, it is known that a volume-fraction in the range from 0.4 to 0.6 results in negative Poisson's ratio in a compressed, collapsed state that is associated with buckling of the periodic topology via global rotational deformation.[17] Inspired by such outcomes, this research creates a double porous metamaterial (referred to as MM) geometry as seen in Fig. 1(a). The geometry may be regarded as an extrusion of a 2D periodic porous frame, such that the cross section is constant through the extruded thickness. When compressed to small extent, the structure exhibits a rotation pattern shown in Fig. 1(b). To fabricate the MM, first a 50.8 mm thick polyurethane foam (Foam Factory, Inc., Macomb, MI) is shaped in a laser cutter (Full Spectrum Laser H-Series 20×12, Las Vegas, NV) into a rectangular cross section 64×80 mm^2 with periodic circular voids of diameter 10 mm, arrayed in a square grid having seven and four voids in the horizontal and vertical spans, respectively. The center-to-center distance between circular voids is 12.7 mm. For purposes of later applying compression constraints in the impedance and TL tube experiments, a 6 mm diameter half-cylinder is cut into each rectangular piece, along the vertical dimension of the photograph in Fig. 1(a). The purpose of the center hole composed from these two half-cylinders is emphasized in Sec. III C. Two such pieces of poroelastic and architected foam are then bonded together with a sufficient but not excessive quantity of spray adhesive. Then, the resulting metamaterial specimen is shaped
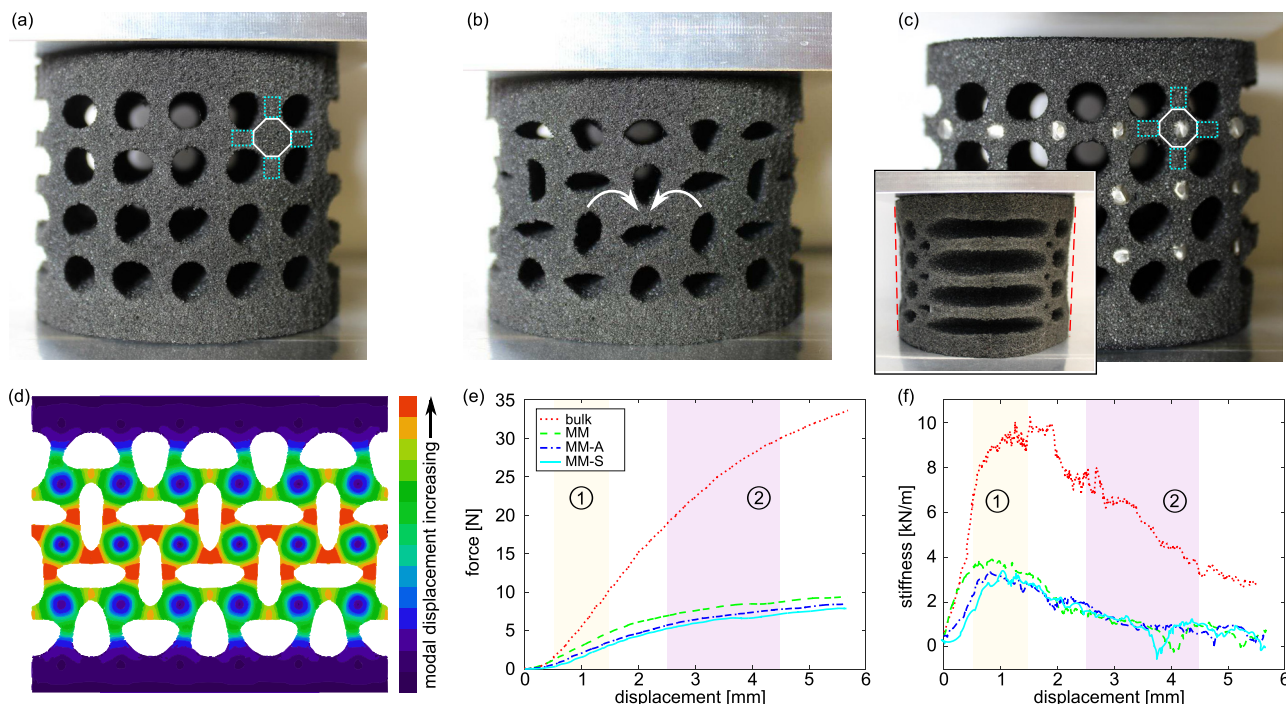

FIG. 1. (Color online) (a) Uncompressed metamaterial (MM) and (b) slightly compressed MM exhibiting rotation. (c) Uncompressed metamaterial with steel rod inclusions (MM-S) and a side view of MM-S at the bottom left. (d) Finite element model result showing eigenmode deformation characteristics associated with (b) at 646.16 Hz. (e) Force-displacement, and (f) stiffness-displacement measurements of bulk foam (bulk,dotted), metamaterial without inclusion (MM, dashed), metamaterial with aluminum inclusion (MM-A, dashed-dotted), and metamaterial with steel inclusion (MM-S, solid).

Shichao Cui and Ryan L. Harne

into a cylinder of 80 mm diameter using a bandsaw, as shown in Fig. 1(a). The 80 mm diameter of the specimen is selected so as to be compatible with the acoustic experiments of this research that take place in rigid wall tubes of internal diameter 77.5 or 79 mm, thus, providing for a mild amount of needed circumferential compression.

The metamaterial specimens with mass inclusions are fabricated in similar ways. When shaped in the laser cutter, in addition to the void pattern described above, voids of diameter of about 3 mm are also cut, arrayed in a grid 6 × 3 in horizontal and vertical spans, respectively. Into these voids are placed aluminum (McMaster-Carr, 8974K21, Ohio) or steel (McMaster-Carr, 89535K43, Ohio) rods cut in lengths to match the corresponding extrusion dimension. A metamaterial with steel inclusions (MM-S) is shown in Fig. 1(c), while metamaterial specimens with aluminum inclusions (MM-A) have identical cross-section geometry. A side view of MM-S is provided at the bottom left of Fig. 1(c) to emphasize that the rod inclusions promote a lateral contraction, the influences of which are discussed in Sec. III D. Minor deviations in specimens' shapes exist due to tolerances of the laser and bandsaw shaping processes that are not suspected to significantly impact the experimental results. The rotational behavior of the compressed MM is exemplified in FE model results shown in Fig. 1(d), in agreement with the experimental observation Fig. 1(b). Full computational modeling details are provided in Sec. III B.

A. Mechanical properties

To examine the mechanical properties of the metamaterials, load frame experiments are conducted (Mark-10 ES20 frame, New York, PCB 1102-05A load cell, New York, Micro-Epsilon ILD 1700-200 laser displacement sensor, Ortenburg, Germany). Three metamaterials and a sample of the bulk foam, of the same overall 80 mm diameter and 64 mm height, are tested (sampling frequency 256 Hz). Multiple cycles of compression and release are applied prior to recording data in order for the specimens to obtain a repeatable seat position in the load frame mounts. Figures 1(e) and 1(f) show force- and stiffness-displacement results of bulk, MM, MM-A, and MM-S specimens. It is clear that bulk foam is stiffer than the metamaterials, such as shown in Fig. 1(f) around displacement 1 mm. A trend of reduced stiffness for increased force, a softening effect, is observed for both bulk foam and metamaterials. As highlighted by the shaded areas in Figs. 1(e) and 1(f), area 1 corresponds to a compression displacement range where the deformation remains relatively linear with finite one-dimensional material stiffness. In contrast, for the area 2 as labeled in Figs. 1(e) and 1(f), the compression range induces nonlinear softening stiffness behaviors for the specimens, associated with collapse either of meso- or microscale pores in the specimens. Yet, the explanations for such softening stiffness features are distinct comparing bulk and metamaterial specimens. For open-cell polyurethane foam, the microscale structure itself buckles under moderate compression giving rise to a softening stiffness trend.[21] In Fig. 1(f), the reduction of the stiffness associated with the buckling of the bulk specimen occurs

around 2 mm displacement. In contrast, for the metamaterials the mesoscale geometry rotates according to a collapsing phenomenon, as shown in Fig. 1(b), which occurs around 1 mm in displacement because the stiffness begins to reduce near this compression region. In addition, the collapsing metamaterial exhibits negative Poisson's ratio, seen comparing Figs. 1(a) and 1(b), as well as much less stiffness than the bulk foam for smaller compression constraints. Such significantly different tailoring of mechanical properties for the same compression sequence indicates that the metamaterials may cultivate more substantial control over acoustic wave propagation characteristics.

III. ADAPTING BROADBAND ACOUSTIC ENERGY ATTENUATION CHARACTERISTICS

A. FT experimental methods and results

Having established a comparison of the mechanical properties, the dynamic responses are then investigated. Considering the low frequency dynamic response,[22] the adaptation of FT is evaluated according to different mass inclusions and compression constraints. Thus, these experiments characterize the elastic wave propagation through the specimens of finite specimens under long wavelength excitation conditions, where the wavelength is significantly greater than the specimen dimensions. The experimental setup to characterize the FT is schematically shown in Fig. 2(a) with a corresponding photograph in Fig. 2(b). A broadband noise signal is delivered to a vibration controller (Vibration Research VR9500, control accelerometer PCB 333B40, New York) after which the signal is amplified (Crown XLS-1500, Elkhart, IN) so as to drive an electrodynamic shaker (LDS V408, Nærum, Denmark). Two force transducers (PCB 208C01, New York) are mounted upstream of and downstream from the specimen, which is held between force expanders that apply a uniformly distributed force over the specimens, as shown in Fig. 2. Data from the transducers is recorded with a sampling frequency of 8192 Hz, while 60 transfer functions (TFs) are averaged from the bandpass filtered data to compute each linear FT TF. This significant amount of data and thorough averaging is anticipated to yield statistically viable data for the specimens examined.

To study the influence of static compression, each metamaterial specimen is evaluated under three conditions of static compression between the force expanders. The dynamic forces delivered from the shaker are therefore centered around such static compression states. Compressed states of about 3 and 6 mm are considered, in addition to a negligibly compressed state, which is termed "uncompressed" hereafter. The shaker location is manually adjusted to achieve these displacement changes, which necessitates the approximate compressed states nominally around 3 and 6 mm. Because a minor amount of compression is required to hold the specimen between the force expanders when subjected to the dynamic force, no truly uncompressed state may be evaluated. For the bulk foam specimen, due to its much higher stiffness compared with metamaterials, static compressions of about 0.6 and 1.1 mm are provided, in addition to the effectively uncompressed state. The local linear stiffnesses of all
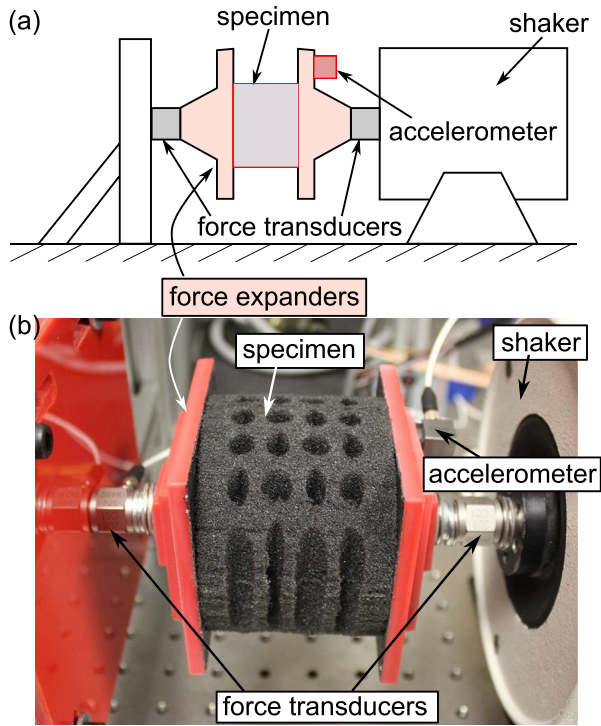
FIG. 2. (Color online) (a) FT experimental setup schematic. (b) Experiment setup photo.

specimens when constrained under such static displacements are shown in Fig. 1(f). For the bulk specimen, it is seen from Fig. 1(f) that the system operates under a pre-buckling regime for both compressed configurations, while all of the metamaterials are in slightly and moderately post-buckled configurations (with very low stiffness) when subjected to compressions of about 3 and 6 mm.

Figure 3 presents the FT for the four specimens according to the frequency and for the three cases of static compression. From Fig. 3(a), it is found that the TF increases almost uniformly across the frequency range for the bulk foam once compressed. For instance, around 800 Hz, the TF for the foam when compressed by 1.15 mm is about 5 dB greater than the TF when uncompressed at the same frequency. This dB difference corresponds to more than three times change of force amplitude. In addition, from about 50 to 260 Hz the TF for the bulk foam increases by ~1 dB due to the same compression, which is relatively small at any given frequency but statistically significant due to its occurrence over such a broad range of low frequencies.

In contrast to the bulk foam for the three metamaterials the TF results shown in Figs. 3(b)–3(d) reveal that the compressed configurations exhibit reduced TF, which is especially clear from about 50 to 400 Hz. For instance, the MM-A undergoes a uniform decrease in TF of about 1 to 3 dB in this frequency range. In fact, these outcomes appear similar to an increase in broadband damping by virtue of increased static compression. Because the double porosity metamaterials may undergo a buckling and collapse behavior, associated with the rotation behavior shown in Figs. 1(b) and 1(d) around compressed states of 1–3 mm, the static stiffness reduction seen in Fig. 1(e) corresponds to a hypothetical

increase in damping properties. This is similar to the "hyperdamping" phenomenon examined in recent research on elastic metamaterials for impact and vibroacoustic energy control[19,20,23] where damping is amplified when structural or material systems are loaded near a critical point. Thus, the increased compression range considered here statically strains the metamaterials toward smaller and smaller stiffness, and thus nearer to a critical point, which increases effective damping properties and reduces broadband FT. Although the absolute levels of the broadband TF reduction are not extraordinarily large, the wide range of frequencies across which the reductions occur in a uniform way emphasize the statistical significance of the phenomenon.

Studying the TF results in further detail, using the −30 dB noise floor lines in Fig. 3 as reference, it is seen that the TFs for the bulk foam, MM, MM-A, and MM-S approximately reach this level, respectively, around 1200 Hz, 900 Hz, 480 Hz, and 400 Hz. As Figs. 3(c) and 3(d) show, the TFs of MM-A and MM-S have similar behavior in TF from about 600 to 1500 Hz, and similarity is also observed by comparing Fig. 3(b) and Figs. 3(c) and 3(d) for the MM and MM-A/S, respectively, from 1200 to 1500 Hz. These similarities occur after each specimen reaches the −30 dB TF level following rapid declines of the TF in the frequency range around 200–600 Hz. The −30 dB level is so small that it approaches the noise floor for measurement. Consequently, the similarities observed among the TFs for MM, MM-A, and MM-S specimens once the levels reach the −30 dB line may be associated with the experimental setup of the force expanders mounted to the up- and downstream force transducers.

Because reduction of the TF level corresponds to less elastic wave energy transfer, it is seen that MM-S in Fig. 3(d) provides the best broadband wave energy absorbing ability, regardless of the static compression level. In addition, the MM-S results in a more rapid decline of the TF level for the same increase in the frequency, when compared to the roll-off rate of the bulk foam and other metamaterials in Figs. 3(a)–3(c). Yet for both the MM-A and the MM-S, the significant suppression of elastic wave energy by the introduction of mass, when compared to the bulk foam and MM, is readily explained by the principles of vibration isolation.[24] In other words, the mass inclusions result in a reduction of the lowest order mode eigenfrequency associated with bulk motion of the interior metamaterial architecture. On the other hand, the reasons for why the MM provides enhanced, broadband reduction of force transmission compared to the bulk foam are more intricate. One explanation is that the double porosity of the metamaterial results in effective masses and springs associated with the remaining poroelastic foam after shaping,[18] A set of such effective masses and springs are highlighted with solid and dotted outlines, respectively, in Fig. 1(a). Thus, the shaping process leads to reductions in local metamaterial stiffness (i.e., the effective springs) so that resonant-like phenomena are possible due to the remaining mass. The full details regarding such enhanced, broadband elastic wave energy suppression provided by the new MMs remain part of ongoing study.
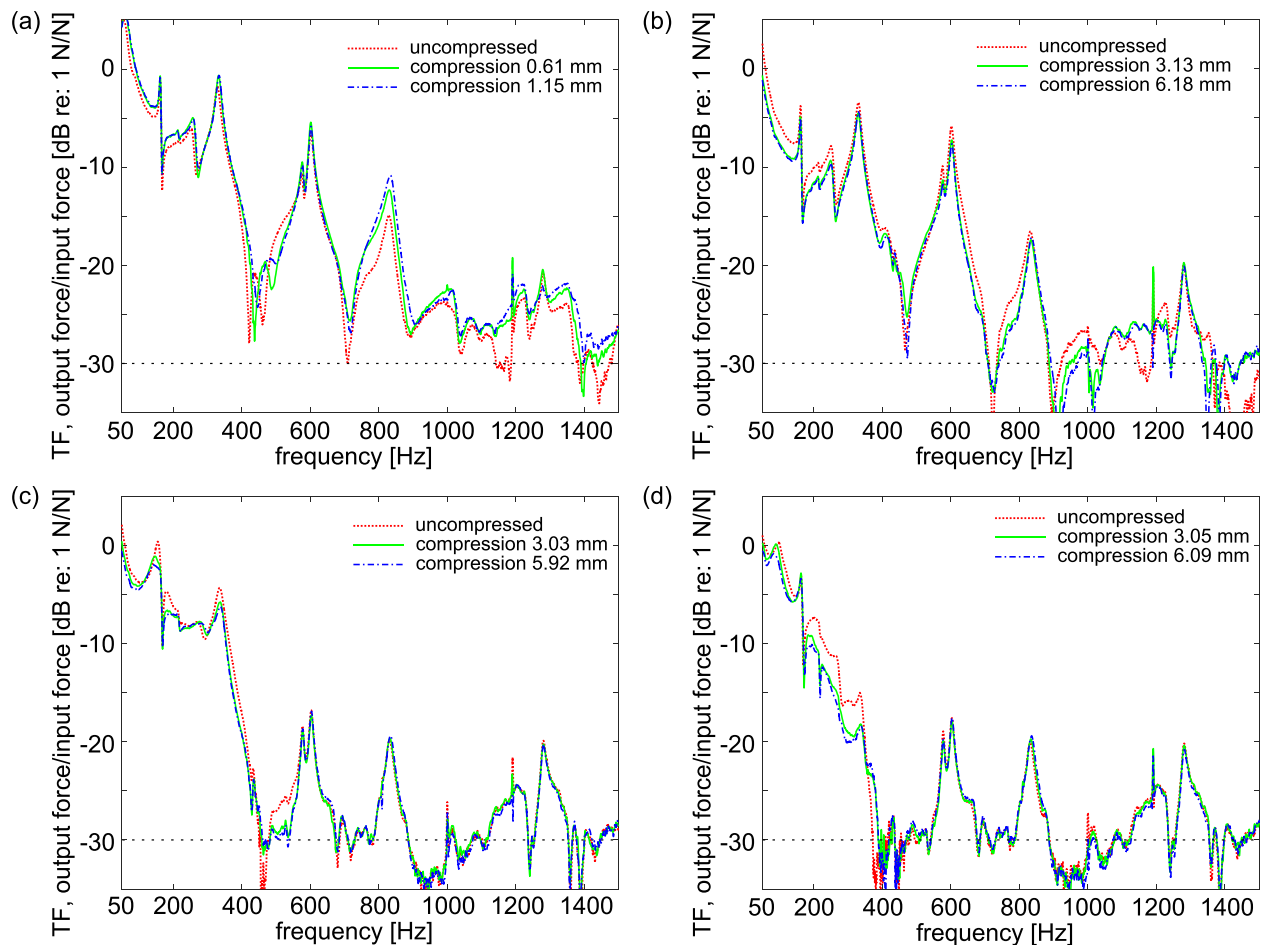
Shichao Cui and Ryan L. Harne

FIG. 3. (Color online) FT for uncompressed conditions (dotted curves), compressed conditions (solid curves), and more compressed conditions (dashed-dotted curves). Each sub-figure legend indicates the specific extent of static compression. Results are shown for the (a) bulk foam, (b) metamaterial without mass inclusion MM, (c) metamaterial with aluminum inclusion MM-A, and (d) metamaterial with steel inclusion MM-S. A reference dash line at −30 dB is shown for ease in visualization.

Figure 4 consolidates key outcomes of the TF results. Figures 4(a) and 4(b) show the TF of uncompressed configurations of bulk foam (dotted), MM (dashed), MM-A (dashed-dotted), and MM-S (solid) in (a) narrowband, and (b) 1/3-octave band. It can be seen from Fig. 4(b) that across the broad bandwidth 250–1200 Hz, the MM-S leads to the lowest TF, while the metamaterials with mass inclusions provide better wave suppression than the bulk foam and MM across the whole range 400–1200 Hz. Cumulative 1/3-octave band FT TF in the frequency ranges 62.5–250 Hz and 250–1000 Hz are presented in Figs. 4(c) and 4(d), respectively. In each sub-figure, four sets of data are shown corresponding to the four specimens. Each dark-shaded left column is the uncompressed and while each light-shaded right column is the most statically compressed state of the respective specimen. In all cases shown in Figs. 4(c) and 4(d), introducing the static compression to the metamaterials uniformly reduces the broadband measure of TF, while for the bulk foam the force transmitted increases. In the lower frequency range 62.5–250 Hz, as shown in Fig. 4(c), the MM has the smallest overall TF, which is explained from the narrowband data of Fig. 3(b) that the magnitudes of the lowest frequency modes of TF are less than the other specimens. Compared to the attenuation achieved by the bulk foam in

this low frequency range of 62.5–250 Hz, the uncompressed MM attenuates the TF by 4 dB more than the uncompressed bulk foam does. And for the compressed conditions of the two specimens, the TF of the MM is 8 dB less than the bulk foam. For the higher frequency range of 250–1000 Hz, the compressed MM-S reduces the transmitted force by 8.26 times more than the reduction provided in the uncompressed state. Interestingly, the MM-S is the only specimen that provides a cumulative TF from 250 to 1000 Hz that is negative in dB, indicating that the MM-S has the ability to attenuate broadband vibroacoustic energy while the compression enhances this capability by about 3 dB. Although the MM-A has smaller narrowband TF than the MM over the frequency range 400–1200 Hz as shown in Fig. 4(b), these two specimens yield similar cumulative FT in the range 250–1000 Hz, seen in Fig. 4(d). This is explained because the TF values around 250 Hz and 400 Hz are similar between them, and due to the logarithmic nature of the dB scale the cumulative sum over 250–1000 Hz is weighted to the large FT contribution from the larger-valued quantities. As it pertains to deploying such double porosity metamaterials in practice, overall energy passed through the metamaterials is of relevance for many applications. As a result, it may be concluded from these experimental results that the MM and
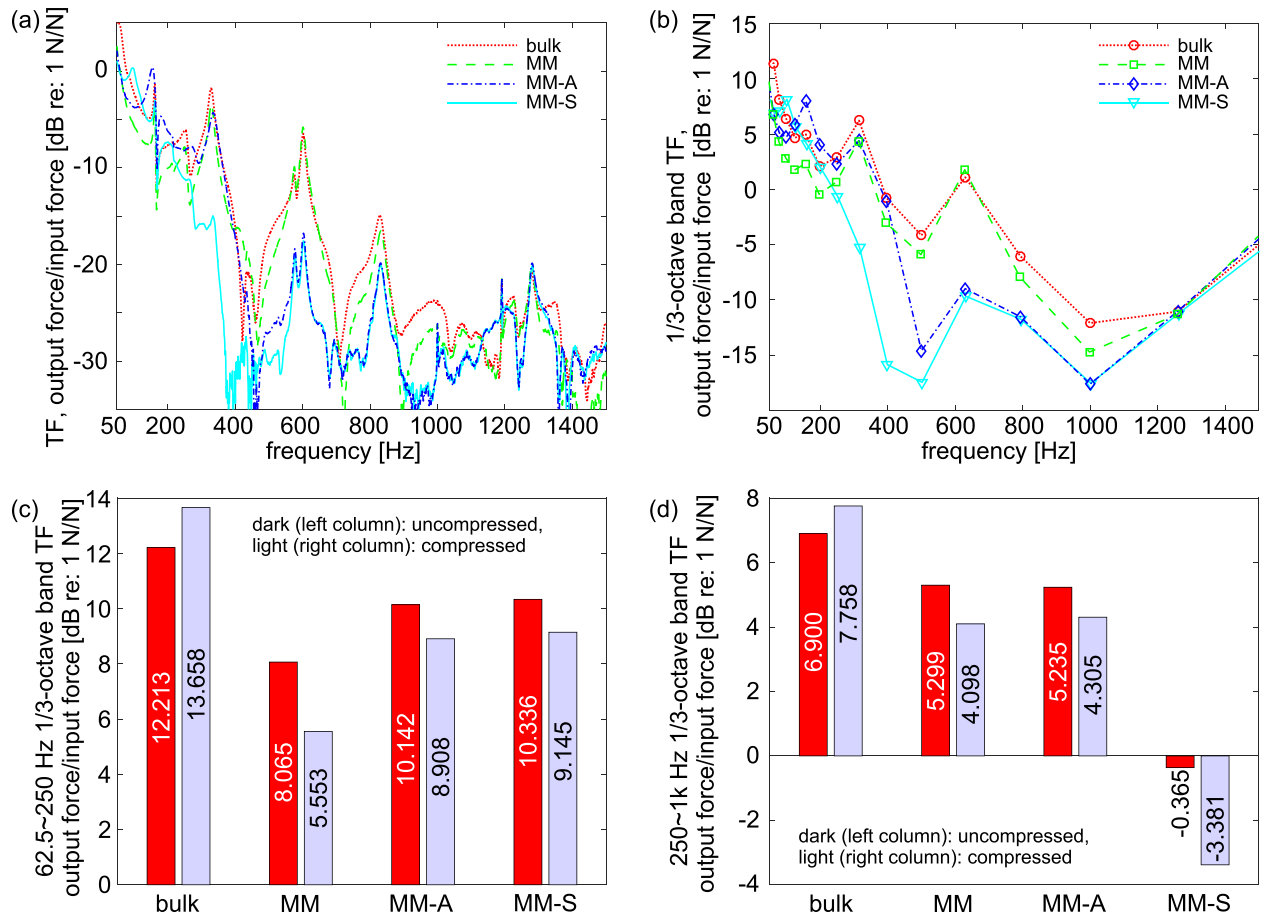
FIG. 4. (Color online) In (a) and (b) are FT TF for bulk foam (dotted curves), MM (dashed curves), MM-A (dashed-dotted curves), and MM-S (solid curves) for uncompressed conditions. (a) Presents narrowband results and (b) presents 1/3-octave band results. Overall 1/3-octave band TF results from (c) 62.5 to 250 Hz and (d) 250 to 1000 Hz. Dark shaded columns denote uncompressed condition results, while light-shaded columns denote most compressed condition results. Compression extents indicated in Fig. 3 legends.

MM-A provide comparable broadband FT reduction from 250 to 1000 Hz, while the MM achieves this with 88% less mass than the MM-A.

B. Computational modeling of absorption coefficient and TL

The influence of static compression levels on the acoustic properties of the double porosity metamaterials is then examined. As shown and discussed in Secs. III C and III D, the boundary conditions of the specimens are critical toward the conclusions drawn from the resulting acoustic properties data. Because it is easier to achieve the ideal boundary conditions for the bulk foam specimen since it does not contract when compressed, only the metamaterials—which contract by negative Poisson's ratio—are hereafter considered to assess TL and absorption coefficient in order to provide a fair comparison. 2D plane strain FE models (COMSOL Multiphysics, Stockholm, Sweden) are constructed using poroelastic and acoustic physics for accurate characterization of the coupled physical domains. The models are created to either compute TL or absorption coefficient. To account for the statically compressed configurations, a stationary model, which is statically compressed by 6 mm, is created to obtain the compressed geometry, which is then provided to the acoustic characterization models, similar to

the method described in Ref. 9. The parameters used to model polyurethane foam are listed in Table I. Young's modulus and density are determined empirically, while the remaining parameters are identified from available literature regarding similar foam materials.[25] In the TL FE models, areas of air (in the 2D plane strain system) are modeled on the incoming and outgoing sides of the specimen whose cross-sectional geometry is modeled exactly, according to the incoming normally incident unit-valued plane wave excitation P_{in}, as shown in Fig. 5(a). A perfectly matched layer is appended to the other side of the outgoing air region to simulate anechoic termination. For metamaterial specimens, the double porous voids in the cross-sectional areas are modeled as air domains. Following the frequency domain study, the averaged pressure P_{out} is measured on the outgoing surface of the air layer at each frequency, so that the TL is computed using

$$\text{TL} = 20 \log\left(\left|\frac{P_{in}}{P_{out}}\right|\right). \tag{1}$$

In the FE model used to compute the absorption coefficient, a normally incident unit-valued plane wave P_{in} travels through a region of air so as to impinge on the specimen, which is terminated with a fixed boundary on the side

4720   J. Acoust. Soc. Am. **141** (6), June 2017

Shichao Cui and Ryan L. Harne

TABLE I. Material properties used in FE models.

Material	Young's modulus (Pa)	Density (kg/m³)	Poisson's ratio	Porosity
Polyurethane	1.176×10^6	31.8	0.44	0.96
Polyimide	6×10^5	9.6	0.45	0.45
Aluminum	72×10^9	2100	0.33	—
Steel	210×10^9	7800	0.30	—

Material	Permeability (m²)	Tortuosity	Biot-Willis coefficient
Polyurethane	1.4×10^{-9}	1.29	0.99
Polyimide	0.2×10^{-9}	3.25	0.45

opposite to the incident wave, as shown in Fig. 5(b). The complex average sound pressures X and Y are, respectively, computed at each frequency at the locations of the virtual microphones 1 and 2 indicated in Fig. 5(b), which simulate the experimental microphones locations. The complex TF is computed at each frequency using

$$H = \frac{G_{xy}}{G_{xx}} = \frac{XY^*}{XX^*}, \tag{2}$$

where "*" denotes the complex conjugate. The complex reflection coefficient R is then determined from

$$R = \frac{H - e^{jkS}}{e^{-jkS} - H} e^{-j2k(l+S)}, \tag{3}$$

where k is the wavenumber, S is the distance between mics 1 and 2, and l is the distance from mic 2 to the upstream surface of the specimen. Consequently, the absorption coefficient is computed by

$$\alpha = 1 - |R|^2. \tag{4}$$

For both FE models, the specimen boundaries are allowed to slide only in the sides parallel to the direction of wave propagation. This boundary condition is challenging to mimic in practice, as discussed in Secs. III C and III D, although it is the ideal boundary condition realization according to the testing standards.

C. TL FE and experimental results

Experiments of TL are carried out alongside the FE studies. The ASTM E2611-09 (Ref. 26) is followed using a TL tube of 77.5 mm internal diameter, four microphones (PCB 130E20, New York), and with the two load method using open and anechoic end terminations. The schematic is shown in Fig. 5(c). White noise is generated by the data acquisition computer and then fed through an amplifier (AudioSource AMP 100, Oregon) to a source speaker at the incoming side of the TL tube setup. The sampling frequency for data is 65 536 Hz, while the digitally filtered data from 40 to 3000 Hz are then used with 80 averages employed for each TL computation. To statically compress the specimen within the tube, two pieces of thin and highly perforated acrylic are made by laser cutting, as presented in Fig. 5(e) at left. Then, the acrylic pieces are applied to the incoming and

outgoing sides of the specimens and connected together through the interior laser cut center cylinder, pointed out by the arrow in Fig. 5(e), using an elastic band. By stretching
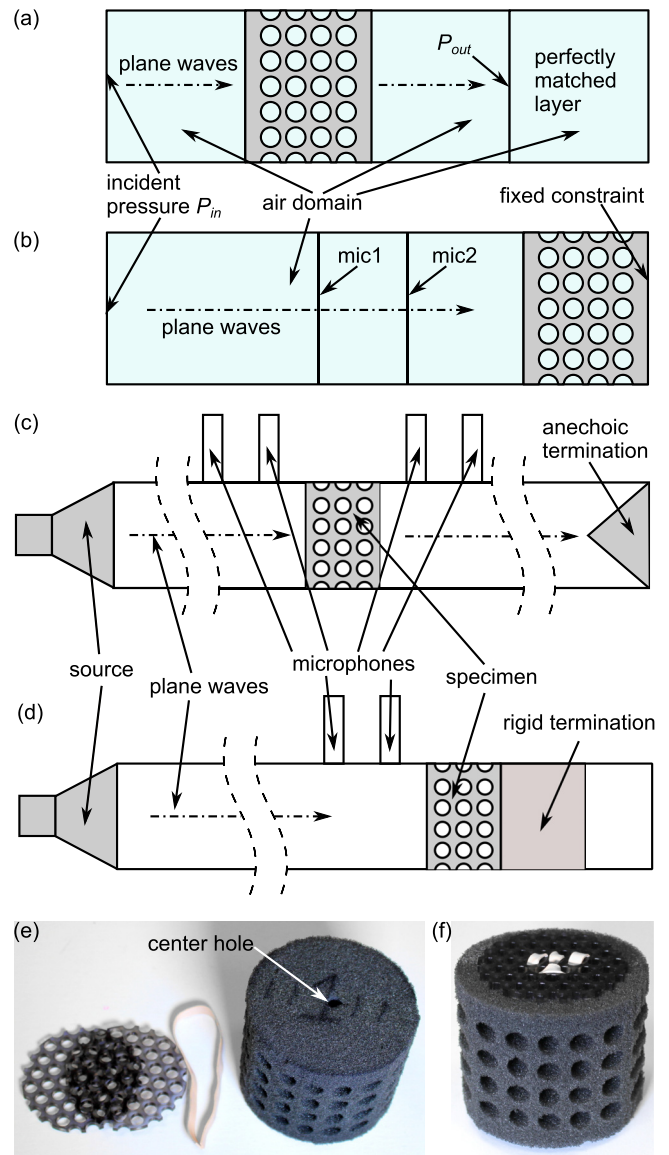

FIG. 5. (Color online) Finite element model schematics of (a) TL and (b) absorption coefficient. Experimental setup schematics of (c) TL and (d) absorption coefficient. (e) Perforated acrylic pieces and an elastic band for applying of constraint, and a top view of MM denoting the center hole for the elastic band to go through. (f) Uncompressed MM with acrylic pieces and elastic band.

the band to different extents, uniform static compressions are realized. The acrylic pieces are slightly smaller than the internal diameter of the tube so as to not interfere with the boundary conditions of the specimens. By their design, all specimens are slightly compressed circumferentially in the tubes in order to prevent direct leakage of sound around the specimens under ideal circumstances. For uncompressed conditions, the acrylic pieces and elastic band are also applied although the band is not stretched, so as not to compress the specimen. The uncompressed condition of the MM using the acrylic pieces and elastic band is shown in Fig. 5(f). By use of the elastic bands, the compression constraints are equal stress rather than equal displacement, where the latter approach is realized in the FT experiments. In the acoustics experiments of compressed conditions, a static compression of around 2 mm is applied, while the circumferential constraint on the specimen introduced by the tube increases the effective compression on the metamaterial specimens to a value closer to 6 mm. Consequently, in the FE model a 6 mm compression is applied.

TL experimental and FE model results are shown in Figs. 6(a) and 6(b) and Figs. 6(c) and 6(d), respectively. Uncompressed and compressed states are compared between Figs. 6(a) and 6(c) and Figs. 6(b) and 6(d). In Fig. 6(a), the

FE model predicts that the mass inclusions enhance the TL from about 50 Hz to 600 Hz, as seen considering the MM-A (solid) and MM-S (dashed-dotted) to the MM (dotted). Interestingly, the TL frequency dependence is not greatly affected whether the mass inclusion is aluminum or steel. When the metamaterials are compressed, the Figs. 6(a) and 6(b) show that the narrowband reduction of TL around 700 Hz shifts to higher frequencies, shown by the arrows in the figures. This outcome agrees with the influence of compression on the TL of glass fiber based materials that were considered on practical grounds.[11] In the experimental results of Figs. 6(c) and 6(d), the narrowband reduction of TL for the MM-A and MM-S is also increased in frequency due to compression, in agreement with the FE model results. The solid arrow in Figs. 6(c) and 6(d) highlights the change in this frequency range of reduced TL for MM-S, which shifts from around 1100 Hz to 1700 Hz due to compression. A similar outcome occurs for MM-A but due to the higher frequencies involved with respect to the cut-off of the TL tube, the reduction in TL for the compressed MM-A in Fig. 6(d) exists beyond the frequencies that may be measured.

While there is reasonable agreement in the computational and experimental results of TL for the MM, considering all parts of Fig. 6, the agreement is not as strong between the FE
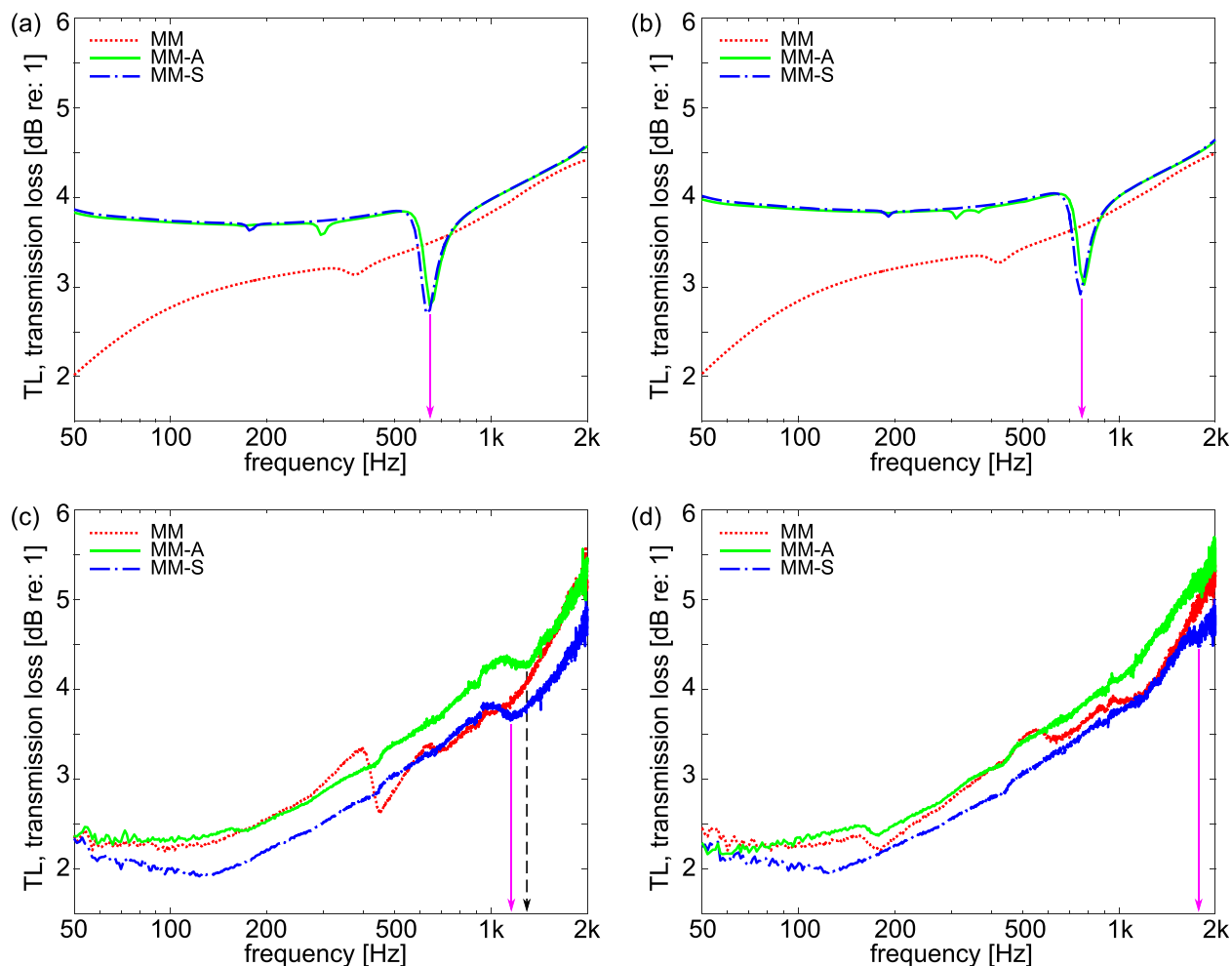

FIG. 6. (Color online) FE and experimental results of TL for MM (dotted curves), MM-A (solid curves), and MM-S (dashed-dotted curves). (a) and (b) show FE results, while (c) and (d) show experimental results, correspondingly in (a) and (c) uncompressed configurations, (b) and (d) statically compressed states.

and experimental findings for MM-A and MM-S at lower frequencies, such as around 50–500 Hz. Indeed, it has been established that ideal boundary conditions are challenging to realize for TL measurements,[27,28] and idealized computational models do not take into account such circumstances. Further discussions to compare the computational and experimental findings are provided at the end of Sec. III D.

Figure 7(a) consolidates the FE uncompressed (dotted), FE compressed (dashed-dotted), experimental uncompressed (dashed), and experimental compressed (solid) TL results for the MM. The FE model predicts that TL increases from around 2.0 to 4.5 dB over the frequency range considered, while the measured increase is around 2.3 to 5.5 dB. Narrowband reductions in the TL occur in the FE results, and the compression induces an increase in the frequency of this feature, shown by the solid arrows in Fig. 7(a). The same trend of compression on the TL provided by the MM is observed experimentally, highlighted by the dashed arrows, albeit at higher frequencies overall. While the FE model predicts a slight and uniform increase of the TL across the whole bandwidth due to compression, the experimental measurements only uncover increased TL from around 400 to 1000 Hz in consequence to the compression. Overall, both the computational and experimental results indicate that compression primarily tailors the TL in the frequency range around 100 to 1000 Hz, clearly revealing that the double porosity metamaterial acoustic characteristics may be tuned by static pre-compression in a frequency region of significance for many applications.

D. Absorption coefficient FE and experimental results

Acoustic waves incident upon a finite-dimensioned impedance interface are either reflected or absorbed, in the general use of the latter term. Having studied the roles of compression on the TL properties of the double porosity metamaterials as a finite and open-backed material layer, the absorption coefficient of the same specimens with fixed-back is then studied to characterize energy loss according to the internal dissipation mechanisms. Experiments are

conducted using an impedance tube, schematically shown in Fig. 5(d), with two microphones (PCB 130E20, New York), and in accordance to ASTM E1050-12.[29] The remaining excitation and data processing features of the TL experiments are replicated in the absorption coefficient examinations, excepting the TF computations.[29]

The results of determining the absorption coefficient α from experiment and FE simulation are shown in Fig. 8. The FE results indicate, as shown in Fig. 8(a), that the mass inclusions primarily cause an increase of α from about 700 to 1600 Hz when compared to the MM. Also, the MM-A provides slightly greater α than MM-S in the narrowband reduction area around 600 Hz for both uncompressed and compressed conditions in Figs. 8(a) and 8(b). The peaks of α around 1300 Hz do not shift significantly due to static compression, as indicated by solid arrows in Figs. 8(a) and 8(b). Experimentally, the results in Figs. 8(c) and 8(d) agree well with the FE outcomes, and plainly reveal that MM-A yields higher α from about 400 to 1000 Hz for both uncompressed and compressed conditions. In addition, a direct comparison of FE predictions of α and the corresponding measurements for the MM is shown in Fig. 7(b). The assessment indicates that the FE model captures the overall measured trend of the absorption coefficient, albeit with a slight frequency shift that may be due to imperfectly known material properties.

Interestingly, the MM-A leads to greater broadband TL and α than MM-S, as indicated in Figs. 6 and 8, which is surprising in light of the mass law.[3] A possible explanation is that this phenomenon is related to the different resonance characteristics of the MM-A and MM-S. Considering the metal rods to be masses, and the polyurethane foam around the masses as equivalent springs, as highlighted in Fig. 1(c), a first approximation of a lower order global-vibration mode of the metamaterial with mass inclusions suggests that the MM-A may resonate around 100 Hz, while the MM-S may resonate at approximately half of this frequency, based on the relative mass increase. As a result, potential resonance-based enhancements to the TL and α measurements may be more prominent for the metamaterial with aluminum
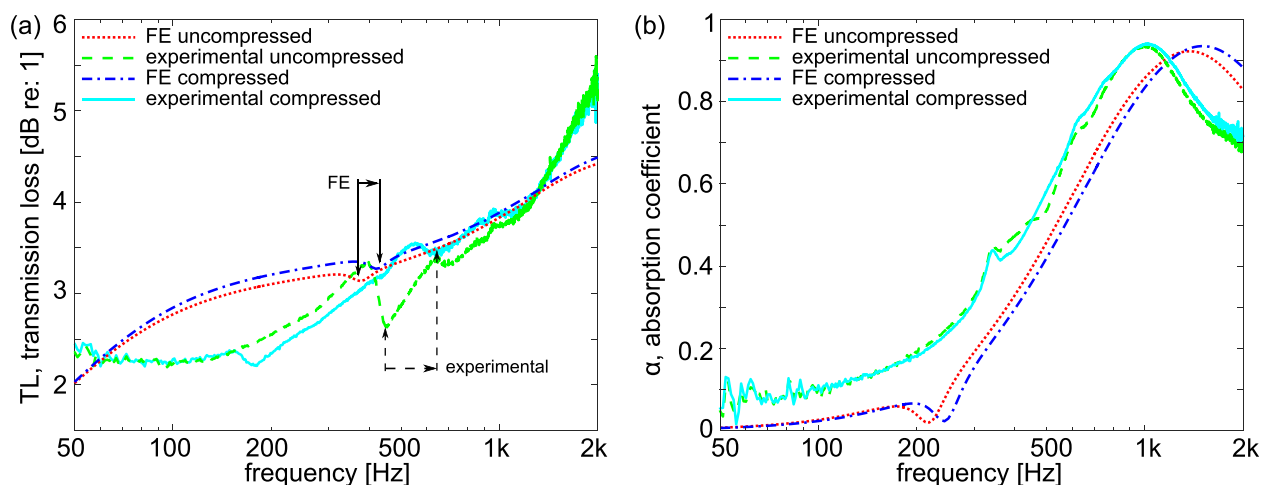

FIG. 7. (Color online) FE and experimental results of (a) TL and (b) absorption coefficient for MM with and without static compression. FE results of uncompressed (dotted curves) and compressed (dashed-dotted curves) states are shown, along with corresponding experimental results of uncompressed (dashed curves) and compressed (solid curves) dates.

J. Acoust. Soc. Am. **141** (6), June 2017
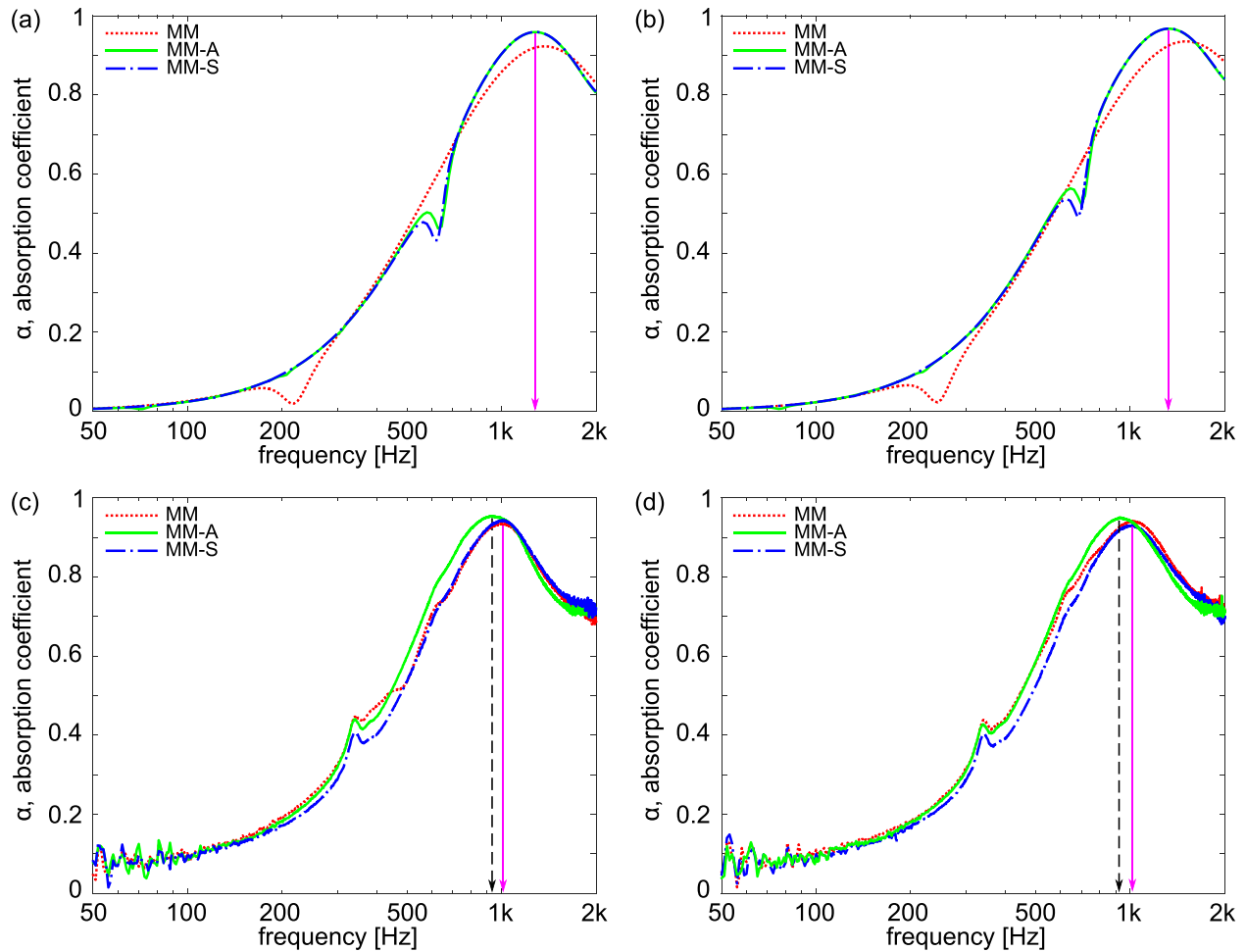
Shichao Cui and Ryan L. Harne   4723

FIG. 8. (Color online) FE and experimental results of absorption coefficient for MM (dotted curves), MM-A (solid curves), and MM-S (dashed-dotted curves). (a) and (b) show FE results, while (c) and (d) show experimental results, correspondingly in (a) and (c) uncompressed configurations, (b) and (d) statically compressed states.

inclusions and steel inclusions since the frequency range associated with these resonances is more fully within the range of frequencies able to be measured in the impedance and TL tubes used here. Indeed, similar results are shown in other work[9] where lightweight polypropylene mass inclusions in polyimide foam yield greater absorption coefficient than steel mass inclusions of the same volume, while the theme of broadband damping growth due to resonant inclusions in damped metamaterials has similarities to the reported "metadamping" phenomenon.[30]

Comparing the FE and experimental results of Figs. 6–8, there are discrepancies that are caused by the challenges of circumferentially constraining the metamaterial specimens. The periodic pattern of circular voids in the metamaterial foam introduces negative Poisson's ratio, which laterally contracts the MM, MM-A, and MM-S specimens when compressed in their vertical dimension, using the orientation shown in Figs. 1(a), 1(b), and 1(c), respectively. It is observed that inserting the metal rods into the foam introduces additional lateral contraction for MM-A and MM-S, as exemplified in Fig. 1(c) at bottom left. These influences result in the potential that the metamaterial specimens are not able to touch the impedance or TL tubes fully around their circumference. Such factors have been the focus of

numerous prior studies where the circumferential constraint[26,27,29] and the shear resonance associated with stiff polyurethane-like foams in TL tubes[31] have been shown to adversely affect measurements of absorption coefficient and TL, particularly at frequencies less than about 1000 Hz. It is evident that discrepancies between the model and experimental results are likely due to these influences, especially for the MM-A and MM-S specimens. It is also possible that the 2D plane strain FE model oversimplifies the extruded three-dimensional (3D) geometry considered experimentally. Nevertheless, the overall trends of tailoring the TL and α characteristics of the double porosity metamaterials by the varied static compression are evident in both the computational and experimental measurements, encouraging the further pursuit of how this concept may be best leveraged.

E. FE study on polyimide metamaterials

Polyurethane foam dissipates considerable acoustic energy when compared to other acoustic materials.[25,32] Thus, tailoring the properties by compression on a double porosity metamaterial created from polyurethane foam may be challenging due to the large inherent dissipation. To explore the capability to control the wave energy absorption
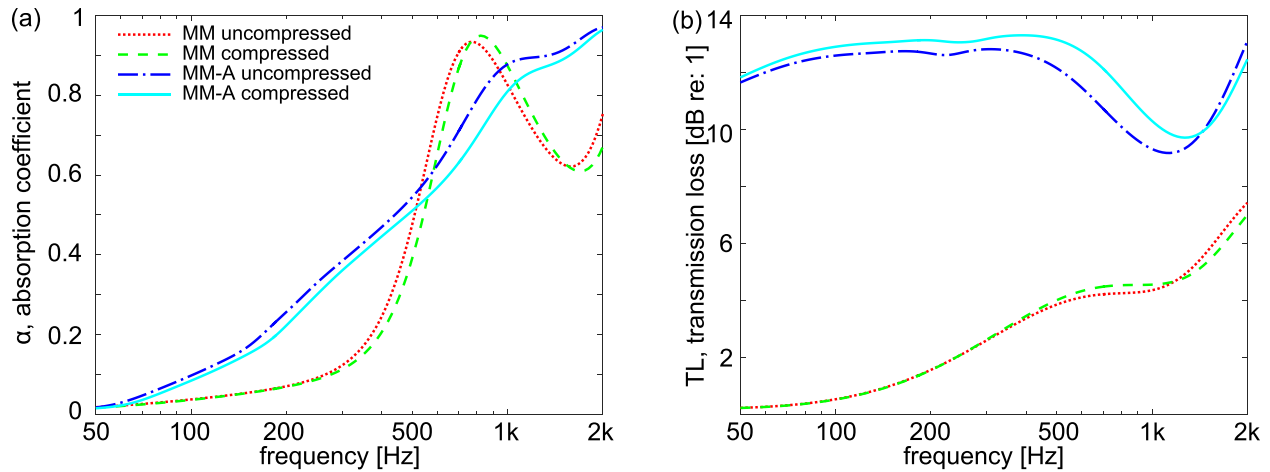
Shichao Cui and Ryan L. Harne

FIG. 9. (Color online) FE results of (a) absorption coefficient and (b) TL using polyimide as the poroelastic material of the metamaterial. Results for the uncompressed/compressed MM (dotted/dashed curves) are shown, along with results for MM-A (dashed-dotted/solid curves).

and transmission characteristics by compression on a double porosity metamaterial composed of a less dissipative media, the FE model is leveraged using poroelastic material properties identified for polyimide foam,[9] and is listed in Table I.

The absorption coefficient FE results are shown in Fig. 9(a). By comparing the uncompressed MM (dotted) and MM-A (dashed-dotted) in Fig. 9(a), it is seen that the mass inclusions cause notable increase in α across the frequency bands 50–500 Hz and 1000–2000 Hz. For much of the low frequency region, the α of the uncompressed MM-A is much greater than the α of the uncompressed MM. For instance, at 300 Hz, the α of uncompressed MM-A is 0.386, and is 0.286 greater than the α of uncompressed MM, which is 0.124, as shown in Fig. 9(a). In addition, the compression upon the MM (dashed) causes the absorption trends to shift almost uniformly to higher frequencies compared to the MM without compression, which is a similar outcome to constraint upon the polyurethane foam-based MM, Fig. 7(b). Although the same influence of compression on the MM-A in Fig. 9(a) is revealed as that for the MM, a more meaningful interpretation is that the overall absorption coefficient for MM-A is reduced due to the compression, since over the whole bandwidth evaluated in Fig. 9(a), the uniform frequency shift is equivalent to a uniform level reduction.

An entirely different influence on the TL by the static compression is observed in the FE predictions shown in Fig. 9(b). Namely, the uncompressed MM-A (dashed-dotted) has a TL that is uniformly and significantly larger than the TL of the MM (dotted), in fact almost 10–12 dB greater over 50–400 Hz, and approximately 5–10 dB greater from 400 to 2000 Hz. These changes are considerable in the perspective of engineering noise control and human sensitivity to sound,[33] suggesting that mass inclusions serve to strongly enhance the TL of the double porosity metamaterial. Moreover, applying compression to the MM-A further enhances TL in the frequency range of 50–1500 Hz. Thus, the choice of poroelastic media for the double porosity metamaterials plays a large influence on the effectiveness of tailoring the wave propagation properties via mass inclusions and compression constraints.

IV. CONCLUSIONS

This research introduced and examined a double porosity metamaterial that tailors acoustic wave energy propagation characteristics by virtue of strategic mass inclusions and compression constraints. It is shown that acoustic properties of absorption coefficient and TL characteristics are not significantly influenced by the presence of a static compression added to the incident wave field on the double porosity metamaterials, although mass inclusions may provide significant and uniform enhancement of the TL. On the other hand, these characteristics are found to be functions of the underlying poroelastic media that composes the metamaterial. For instance, less absorptive media (polyimide foam) are more strongly affected by the compression and mass inclusions than strongly absorptive media (polyurethane foam). In elastic wave propagation experiments, it is seen that the FT is greatly reduced in the low frequency bandwidth by compression applied to the double porosity metamaterials, while similar compression slightly enhances the transmitted force through bulk foam. At higher frequencies, the analogy of the metamaterials as vibration isolators is clear because heavier metamaterials containing mass inclusions provide large and broadband suppression of transmitted force. Compared to prior investigations of resonant inclusions within damped metamaterials,[30] the results of this report reveal that elastic and acoustic wave damping can be enhanced across broad bands of frequencies by utilizing only compression and double porosity, i.e., the MM specimen, while pronounced attenuation of higher frequencies waves may be provided by additional resonant inclusions. These outcomes demonstrate that effective combination of poroelastic material, internal architecture, compression constraints, and embedded mass provide valuable means for controlling acoustic wave propagation characteristics, which may find application in vibration and sound absorbing contexts.

ACKNOWLEDGMENTS

[1]J. F. Allard and N. Atalla, *Propagation of Sound in Porous Media: Modelling Sound Absorbing Materials* (Wiley, Chichester, 2009), pp. 1–349.

[2]L. Goines and L. Hagler, "Noise pollution: A modern plague," South. Med. J. **100**, 287–294 (2007).

[3]L. E. Kinsler, A. R. Frey, A. B. Coppens, and J. V. Sanders, *Fundamentals of Acoustics* (Wiley, New York, 2000), pp. 162–163.

[4]H. Salleh and M. J. Brennan, "Control of flexural waves on a beam using a vibration neutraliser: Effects of different attachment configurations," J. Sound Vib. **303**, 501–514 (2007).

[5]G. Acar and C. Yilmaz, "Experimental and numerical evidence for the existence of wide and deep phononic gaps induced by inertial amplification in two-dimensional solid structures," J. Sound Vib. **332**, 6389–6404 (2013).

[6]E. Baravelli and M. Ruzzene, "Internally resonating lattices for bandgap generation and low-frequency vibration control," J. Sound Vib. **332**, 6562–6579 (2013).

[7]J. P. Groby, C. Lagarrigue, B. Brouard, O. Dazel, and V. Tournat, "Using simple shape three-dimensional rigid inclusions to enhance porous layer absorption," J. Acoust. Soc. Am. **136**, 1139–1148 (2014).

[8]C. Lagarrigue, J. P. Groby, V. Tournat, O. Dazel, and O. Umnova, "Absorption of sound by porous layers with embedded periodic arrays of resonant inclusions," J. Acoust. Soc. Am. **134**, 4670–4680 (2013).

[9]A. C. Slagle and C. R. Fuller, "Low frequency noise reduction using poro-elastic acoustic metamaterials," in *Proceedings of the 21st AIAA/CEAS Aeroacoustics Conference*, Dallas, TX (2015), pp. 2015–3113.

[10]K. Idrisi, M. E. Johnson, D. Theurich, and J. P. Carneal, "A study on the characteristic behavior of mass inclusions added to a poro-elastic layer," J. Sound Vib. **329**, 4136–4148 (2010).

[11]O. Doutres and N. Atalla, "Experimental estimation of the transmission loss contributions of a sound package placed in a double wall structure," Appl. Acoust. **72**, 372–379 (2011).

[12]X. Olny and C. Boutin, "Acoustic wave propagation in double porosity media," J. Acoust. Soc. Am. **114**, 73–89 (2003).

[13]N. Atalla and R. Panneton, "Acoustic absorption of macro-perforated porous materials," J. Sound Vib. **243**, 659–678 (2001).

[14]E. Gourdon and M. Seppi, "On the use of porous inclusions to improve the acoustical response of porous materials: Analytical model and experimental verification," Appl. Acoust. **71**, 283–298 (2010).

[15]F. C. Sgard, X. Olny, N. Atalla, and F. Castel, "On the use of perforations to improve the sound absorption of porous materials," Appl. Acoust. **66**, 625–651 (2005).

[16]J. T. B. Overvelde, S. Shan, and K. Bertoldi, "Compaction through buckling in 2D periodic, soft and porous structures: Effect of pore shape," Adv. Mater. **24**, 2337–2342 (2012).

[17]J. Shim, P. Wang, and K. Bertoldi, "Harnessing instability-induced pattern transformation to design tunable phononic crystals," Int. J. Solids Struct. **58**, 52–61 (2015).

[18]S. Shan, S. H. Kang, P. Wang, C. Qu, S. Shian, E. R. Chen, and K. Bertoldi, "Harnessing multiple folding mechanisms in soft periodic structures for tunable control of elastic waves," Adv. Funct. Mater. **24**, 4935–4942 (2014).

[19]J. Bishop, Q. Dai, Y. Song, and R. L. Harne, "Resilience to impact by extreme energy absorption in lightweight material inclusions constrained near a critical point," Adv. Eng. Mater. **18**, 1871–1876 (2016).

[20]R. L. Harne, Y. Song, and Q. Dai, "Trapping and attenuating broadband vibroacoustic energy with hyperdamping metamaterials," Extreme Mech. Lett. **12**, 41–47 (2017).

[21]V. Shulmeister, M. W. D. Van der Burg, E. Van der Giessen, and R. Marissen, "A numerical study of large deformations of low-density elastomeric open-cell foams," Mech. Mater. **30**, 125–140 (1998).

[22]A. Carrella, M. J. Brennan, T. P. Waters, and V. Lopes, Jr., "Force and displacement transmissibility of a nonlinear isolator with high-static-low-dynamic-stiffness," Int. J. Mech. Sci. **55**, 22–29 (2012).

[23]I. Antoniadis, D. Chronopoulos, V. Spitas, and D. Koulocheris, "Hyper-damping properties of a stiff and stable linear oscillator with a negative stiffness element," J. Sound Vib. **346**, 37–52 (2015).

[24]J. P. Den Hartog, *Mechanical Vibrations* (McGraw-Hill, New York, 1947), pp. 117–121.

[25]R. Panneton and X. Olny, "Acoustical determination of the parameters governing viscous dissipation in porous media," J. Acoust. Soc. Am. **119**, 2027–2040 (2006).

[26]ASTM E2611-09, *Standard Test Method for Measurement of Normal Incidence Sound Transmission of Acoustical Materials Based on the Transfer Matrix Method* (American Society for Testing and Materials, Philadelphia, PA, 2009).

[27]B. H. Song and J. S. Bolton, "Effect of circumferential edge constraint on the acoustical properties of glass fiber materials," J. Acoust. Soc. Am. **110**, 2902–2916 (2001).

[28]D. Pilon, R. Panneton, and F. Sgard, "Behavioral criterion quantifying the edge-constrained effects on foams in the standing wave tube," J. Acoust. Soc. Am. **114**, 1980–1987 (2003).

[29]ASTM E1050-12, *Standard Test Method for Impedance and Absorption of Acoustical Materials Using a Tube, Two Microphones and a Digital Frequency Analysis System* (American Society for Testing and Materials, Philadelphia, PA, 2012).

[30]M. I. Hussein and M. J. Frazier, "Metadamping: An emergent phenomenon in dissipative metamaterials," J. Sound Vib. **332**, 4767–4774 (2013).

[31]J. Kunio, T. Yoo, K. Hou, and J. Enok, "A comparison of two and four microphone standing wave tube procedures for estimating the normal incidence absorption coefficient," in *38th International Congress and Exposition on Noise Control Engineering*, Ottawa, Canada (2009), pp. 1057–1065.

[32]Y. Atalla and R. Panneton, "Inverse acoustical characterization of open cell porous media using impedance tube measurements," Can. Acoust. **33**, 11–24 (2005), available at https://jcaa.caa-aca.ca/index.php/jcaa/article/view/1711.

[33]D. A. Bies and C. H. Hansen, *Engineering Noise Control: Theory and Practice* (Spon, London, 2006), pp. 54–91.